SAND REPORT
SAND2003-1236
Unlimited Release
Printed April 2003

Final Report on LDRD Project: High-Bandwidth Optical Data Interconnects for Satellite Applications

Darwin K. Serkland, Kent M. Geib, Ethan L. Blansett, Gary D. Karpen,
Gregory M. Peake, Terry W. Hargett, Victoria M. Montano, Charles T. Sullivan,
Andrew A. Allerman, Jeffrey L. Rienstra

Prepared by
Sandia National Laboratories
Albuquerque, New Mexico 87185 and Livermore, California 94550

Sandia is a multiprogram laboratory operated by Sandia Corporation,
a Lockheed Martin Company, for the United States Department of Energy's
National Nuclear Security Administration under Contract DE-AC04-94-AL85000.

Issued by Sandia National Laboratories, operated for the United States Department of Energy by Sandia Corporation.

Available to DOE and DOE contractors from
U.S. Department of Energy
Office of Scientific and Technical Information
P.O. Box 62
Oak Ridge, TN 37831

Telephone: (865)576-8401
Facsimile: (865)576-5728
E-Mail: reports@adonis.osti.gov
Online ordering: http://www.doe.gov/bridge

Available to the public from
U.S. Department of Commerce
National Technical Information Service
5285 Port Royal Rd
Springfield, VA 22161

Telephone: (800)553-6847
Facsimile: (703)605-6900
E-Mail: orders@ntis.fedworld.gov
Online order: http://www.ntis.gov/help/ordermethods.asp?loc=7-4-0#online

SAND2003-1236
Unlimited Release
Printed April 2003

Final Report on LDRD Project: High-Bandwidth Optical Data Interconnects for Satellite Applications

Darwin K. Serkland, Kent M. Geib, Ethan L. Blansett, Gary D. Karpen,
Gregory M. Peake, Terry W. Hargett*, Victoria M. Montano*, Charles T. Sullivan
RF Microsystems Technologies Department

Andrew A. Allerman
Chemical Processing Science Department

Jeffrey L. Rienstra
Space Sensor Engineering Department

Sandia National Laboratories
P. O. Box 5800
Albuquerque, New Mexico 87185-0603

Abstract

This report describes the research accomplishments achieved under the LDRD Project "High-Bandwidth Optical Data Interconnects for Satellite Applications." The goal of this LDRD has been to address the future needs of focal-plane-array (FPA) sensors by exploring the use of high-bandwidth fiber-optic interconnects to transmit FPA signals within a satellite. We have focused primarily on vertical-cavity surface-emitting laser (VCSEL) based transmitters, due to the previously demonstrated immunity of VCSELs to total radiation doses up to 1 Mrad. In addition, VCSELs offer high modulation bandwidth (roughly 10 GHz), low power consumption (roughly 5 mW), and high coupling efficiency (greater than –3dB) to optical fibers. In the first year of this LDRD, we concentrated on the task of transmitting analog signals from a cryogenic FPA to a remote analog-to-digital converter. In the second year, we considered the transmission of digital signals produced by the analog-to-digital converter to a remote computer on the satellite. Specifically, we considered the situation in which the FPA, analog-to-digital converter, and VCSEL-based transmitter were all cooled to cryogenic temperatures. This situation requires VCSELs that operate at cryogenic temperature, dissipate minimal heat, and meet the electrical drive requirements in terms of voltage, current, and bandwidth.

* L&M Technologies, Inc.

Acknowledgments

The authors thank C. Andy Boye and Kurt R. Lanes for their technical guidance and support of this activity. We also thank Daniel M. Grasso for measuring the DC performance of cryogenic VCSELs over a range of temperatures from 100 to 300 K. Sandia is a multiprogram laboratory operated by Sandia Corporation, a Lockheed Martin Company, for the United States Department of Energy's National Nuclear Security Administration under contract DE-AC04-94AL85000.

Contents

(This page is left blank intentionally.)

1. Introduction

1.1. LDRD Project Overview

Optical fibers are rapidly replacing electrical cables as the medium of choice for transmission of high-bandwidth analog and digital signals. Coaxial cables cannot compete with the fiber's high bandwidth capacity, low attenuation coefficient, and immunity to electromagnetic interference. Moreover, optical fibers are cheap, reliable, and robust. Finally, for air and space-based applications, optical fibers also offer substantial savings in weight as compared to traditional coaxial cables.

The goal of this LDRD has been to address the future needs of focal-plane-array (FPA) sensors by introducing high-bandwidth optical interconnects to transmit data from a FPA to processing electronics on board a satellite. We have focused primarily on vertical-cavity surface-emitting laser (VCSEL) based transmitters, due to the previously demonstrated immunity of VCSELs to total radiation doses up to 1 Mrad. In addition, VCSELs offer high modulation bandwidth (roughly 10 GHz), low power consumption (roughly 5 mW), and high coupling efficiency (greater than –3dB) to optical fibers. In the first year of this LDRD, we concentrated on the task of transmitting analog signals from a cryogenic FPA to a remote analog-to-digital converter, which typically dissipates too much heat to be located near the cryogenic FPA. We explored whether it is possible to make an optical transmitter that dissipates less heat than conventional electrical transmitters, and simultaneously achieves the required linearity, signal-to-noise ratio, and bandwidth.

In the second year, we considered the transmission of digital signals produced by the analog-to-digital converter to a remote computer on the satellite. Specifically, we considered the situation in which the FPA, analog-to-digital converter, and VCSEL-based transmitter are all cooled to cryogenic temperatures. Low-power-dissipation CMOS analog-to-digital converters are within the realm of possibility. As with the analog transmitter, we considered whether it is possible to make a digital optical transmitter that dissipates less heat than an electronic transmitter. For this task, we fabricated VCSELs specifically for operation at cryogenic temperatures that also featured low threshold current and high electrical-to-optical conversion efficiency. The VCSELs were driven with low-power 3-V CMOS logic circuits, similar to potential low-power analog-to-digital converters.

2. Low-Power Optical Transmitters

2.1. Optical Transmitter Options

An optical transmitter converts electrical drive signals into optical output signals. Two options exist for such transmitters. The first option is direct modulation of a laser by varying its pumping level. Semiconductor diode lasers are the most viable candidates for direct modulation, since they are compatible in voltage (less than 5 V) and current (less than 20 mA) with conventional low-power electronics. Diode lasers are modulated by varying the current above threshold and typically exhibit a linear response of output optical power to input current variations. The two dominant types of semiconductor lasers, edge-emitting lasers (EELs),[1,2] and vertical-cavity surface-emitting lasers (VCSELs) will be considered below.

A second option for an optical transmitter relies on indirect modulation of a laser by an optical modulator that is separate from the laser. Two common types of electrically driven optical modulators are electro-optic modulators (EOMs) and electro-absorption modulators (EAMs).[3] Electro-optic modulators are based on the electro-optic effect, in which an applied voltage changes the refractive index of a material and thereby changes the phase of an optical beam propagating through the material. A Mach-Zehnder interferometer (MZI) modulator achieves amplitude modulation by putting two electro-optic phase modulator sections inside a Mach-Zehnder interferometer. The MZI modulator has a sinusoidal transfer function versus input voltage, which can be considered approximately linear over a small voltage range at the correct bias point. An electro-absorption modulator (EAM) works by changing the absorption of a semiconductor material in response to input voltage. The EAM typically operates over a narrow band of wavelengths near the bandedge of the semiconductor. The transfer function is roughly quadratic versus voltage, but can be considered approximately linear over a small voltage range.

In the following two sections, we will consider in detail the options for both direct and indirect optical modulation. The main objective here is to select a transmitter, for cryogenic operation, that dissipates less power than an electrical transmitter. As a rough guide, we consider the electrical transmitters to dissipate 5 mW each. Other considerations for the optical transmitter are signal-to-noise ratio and linearity of modulation.

2.2. Direct Modulation of Lasers

As mentioned above, the two categories of semiconductor lasers to be considered for direct modulation are edge-emitting lasers (EELs) and vertical-cavity surface-emitting lasers (VCSELs). We focus on AlGaAs-based semiconductor lasers, operating at wavelengths near 850 nm, since these offer the highest performance. Both EELs and VCSELs have similar operating voltages, near 2.0 V, although the VCSEL voltages tend to be slightly higher due to their series resistance values near 100 ohms. Also, both EELs and VCSELs can achieve high electrical-to-optical conversion efficiencies (above 50%).

The main difference between VCSELs and EELs lies in their threshold currents. Low-power VCSELs have threshold currents between 0.1 and 1.0 mA, whereas low-power EELs have threshold currents roughly one order of magnitude larger, between 1 and 10 mA. Since efficiencies are roughly comparable, this means that EELs deliver roughly an order of magnitude more optical power than VCSELs. However, because the output beam from an EEL is typically elliptical, it is more difficult to efficiently couple its output into an optical fiber. Finally we mention that VCSELs readily achieve almost 10 GHz of small-signal modulation bandwidth with less than 1 pF of capacitance. Although special EELs can achieve high bandwidth, EELs typically offer less modulation bandwidth than VCSELs.

The VCSEL is the clear favorite in terms of achieving minimum power dissipation. Figure 2.1 shows the simulated characteristics of a low-power VCSEL having a threshold current of 0.2 mA, a threshold voltage of 1.74 V, a slope efficiency of 0.7 mW/mA, and a series resistance of 200 ohms. Note that at 1.0 mA of current, the input power is 2.0 mW and the output power is over 0.5 mW, yielding a conversion efficiency above 25%. Hence, at 1.0 mA of current, less than 1.5 mW of power is dissipated as heat.

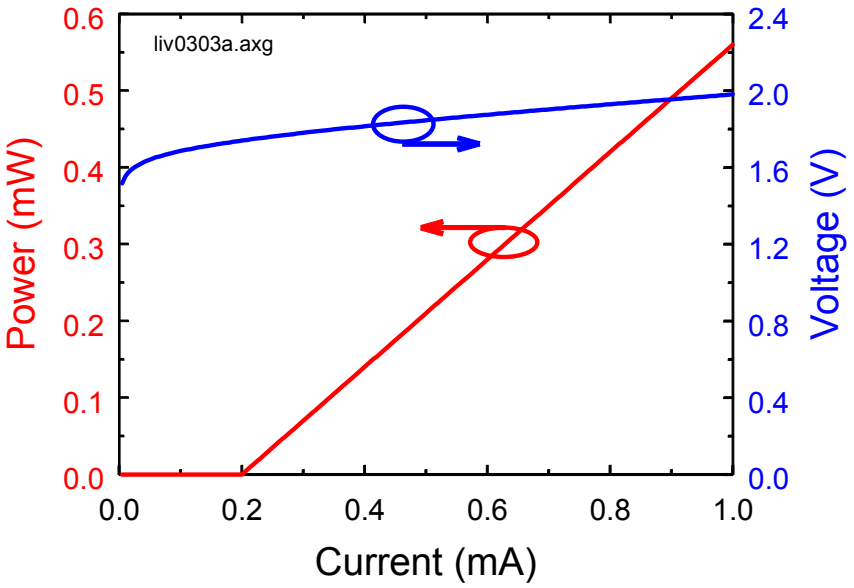

Figure 2.1. Simulated characteristics of a low-power VCSEL, assuming a 0.2-mA threshold current, 1.74-V threshold voltage, 0.7-mW/mA slope efficiency, and 200-ohm series resistance.

2.3. Indirect Modulation using External Modulators

The use of an external modulator for indirect modulation avoids heat dissipation from the laser source, because the laser can be located remotely (away from the cryogenic electronics) where its power dissipation may be tolerated. However, we must realize that any optical absorption in the modulator usually causes heat generation.

Electro-absorption modulators (EAMs) operate by absorbing light in the semiconductor.[4] In order to maximize the signal-to-noise ratio, 100% modulation of the input laser light is desired. Hence, at one extreme, the EAM will absorb roughly 100% of the input light. The circuit that drives the EAM must supply the photocurrent needed to sustain the modulator voltage. A typical EAM based on the quantum-confined Stark effect requires a bias voltage (for example $V_B = 6$ V), to absorb the incident light, and creates a photocurrent $I_{PH} = P_{OPT} / V_P$, where P_{OPT} is the optical power that is absorbed and $V_P = 1.4$ V is the photon energy. A consideration of the band diagram of the reverse biased EAM shows that the total power dissipated as heat is roughly $P_{DISS} = P_{OPT} * (V_B + V_P) / V_P$, which equals roughly 5 times the incident optical power for the bias voltage quoted above.

In order to compare the performance of a modulator to that of a laser, we determine how much power, P_{DISS}, is dissipated to achieve 100% modulation of P_{OPT}. Clearly, the ratio $R_P = P_{OPT} / P_{DISS}$ can be considered as a modulation efficiency to be maximized. For the EAM discussed above, this ratio is $R_P = 0.20$. For a laser, the ratio is $R_P = E_{WP} / (1 - E_{WP})$, where E_{WP} is the "wall-plug" efficiency. For the low-power VCSEL considered in the previous section, the wall-plug efficiency was a bit more than 0.25 at a current of 1.0 mA, yielding a modulation efficiency of $R_P = 0.33$. Hence, the VCSEL dissipates less power than this EAM to achieve an equivalent level of optical modulation. We note that optically resonant EAMs could be engineered to yield improved modulation efficiency. However, in light of their nonlinear transfer function and narrow band of operating wavelengths, we will eliminate EAMs from further consideration.

The Mach-Zehnder interferometer (MZI) modulator appears more attractive than the EAM, because in principle it has zero optical absorption. Ideally, the input light is simply shifted between the two output ports, which would both be routed away from the cryogenic assembly to remote photodiodes. In order to reduce the drive voltage requirement to the 5 V level, waveguide MZI modulators must be fabricated. The main limitation of waveguide devices is that they typically exhibit 6 dB of optical insertion loss due to the difficulty of efficiently coupling the input and output ports to optical fibers. For comparison to the devices above, 6 dB of insertion loss translates into a modulation efficiency of $R_P = 0.33$, which is the same as for the VCSEL with 25% wall plug efficiency.

In addition to optical insertion loss, the MZI modulator also presents a significant capacitive load to the driver circuit, which results in increased power dissipation at high modulation frequencies. For high-frequency performance, the MZI modulator is typically made to have an electrical transmission line with characteristic impedance of 50 ohms. However, driving either a capacitive load or a 50-ohm line to voltages near 5 V requires much more power than an electronic transmitter. Additional considerations are the sinusoidal transfer function, the need for feedback to keep the modulator bias point from drifting, and the additional complexity of having at least one input and two output fibers per modulator.

2.4. Optical Transmitter Conclusions

Direct modulation of VCSELs appears to be the best way to obtain an optical transmitter that dissipates less than 5 mW of power, and provides good modulation efficiency and linearity. We considered a realistic VCSEL example in which more than 0.5 mW of modulated optical power was obtained with less than 1.5 mW of dissipated heat. The modulation efficiency could be improved at higher power levels, but would be sacrificed at lower power levels. The alternatives also have their advantages (and disadvantages) that are summarized below.

The EEL dissipates roughly 10 times more power than the VCSEL, but also provides roughly 10 times more power. Hence, in situations where a power budget of 10 or more mW per channel exists, the EEL will provide roughly 3 times higher signal-to-noise ratio (based on shot noise considerations to be discussed in the following section). The elliptical beam from the EEL is more difficult to couple into an optical fiber than the circular beam from a VCSEL. Finally, we emphasize that both the EEL and VCSEL provide linear transfer functions, which is important for analog transmission.

Indirect modulation of a remotely located laser using an EAM or MZI EOM also appears to be a viable alternative to direct modulation of semiconductor lasers. We have demonstrated that the EAM is only slightly less power efficient than the VCSEL, and we indicated that this could potentially be overcome with optically resonant EAM designs. However, the EAM only operates over a narrow band of wavelengths, which increases the system constraints.

The MZI EOM is attractive because optically it has the potential to be substantially more power efficient than the VCSEL. Although we have not conclusively proven it here, it seems that the capacitive load of realistic MZI EOMs forces them to consume more power than electronic transmitters. The low-loss MZI also requires at least 1 input and 2 output optical fibers, which increases the system complexity. Finally, we mention that both modulator approaches suffer from inherently nonlinear transfer functions, which make them problematic for analog baseband transmission of FPA signals to a remote digitizer.

3. Analog Optical Transmission

3.1. Analog Transmission of FPA Signals

The main goal of the first year of the LDRD was to implement optical transmission of analog signals from a cryogenic focal-plane array (FPA) to a remote analog-to-digital converter. The advantage of this arrangement is that the analog-to-digital converter, which dissipates large amounts of heat, does not need to be cooled. Typically the link between the FPA and the digitizer is electrical. Our exploration of optical links was motivated by a desire to reduce the power dissipation of the transmitter and increase the thermal isolation between the cooled FPA and the outside world. The electrical transmitters dissipate somewhat high powers (at least 5 mW per channel) because they must drive a capacitive cable. Moreover, cables that have good electrical conduction also conduct heat readily from the outside world to the cryogenic FPA. By comparison, an optical fiber does not present a capacitive load to the optical transmitter and is thermally insulating. As a bonus, the optical fiber offers virtually limitless bandwidth capacity, so the pixel rate can be increased to meet future FPA needs.

In the sections that follow, we will first discuss the theoretical limits of signal-to-noise ratio in optical interconnects, imposed by shot noise, and then discuss actual laser and system measurements.

3.2. Shot Noise Considerations

In this section, we consider the signal-to-noise ratio that can be obtained in an optical interconnect, assuming the lasers are shot-noise limited.[5] Although it is possible to reduce laser noise somewhat below the shot-noise limit, with special effort, the technical difficulties involved preclude this from practical consideration.

Lasers are typically characterized by their relative intensity noise (RIN),[6] which can be defined by

$$RIN_P = \frac{1}{SNR_P \times B}, \tag{3.1}$$

where B is the bandwidth of the measurement, and SNR_P is the optical-power signal-to-noise ratio, defined by

$$SNR_P = \frac{P^2}{\Delta P^2}, \tag{3.2}$$

where P is the mean optical power and ΔP^2 is the mean-square value of optical power deviations from the mean. The coherent state generated by an ideal laser exhibits Poisson photon statistics, in which case the mean-square fluctuations are given by the shot-noise formula

$$\Delta P^2 = 2BE_\lambda P \ , \tag{3.3}$$

where E_λ is the photon energy, and the other terms have been defined previously.

As a practical matter, it is convenient to write formulas similar to those above in terms of measured currents from a photodetector, rather than in terms of optical powers. The photocurrent I is linearly related to the incident optical power by

$$I = \Re P = \left(\frac{\eta e}{E_\lambda} \right) P \ , \tag{3.4}$$

where $\Re$ is the responsivity of the photodetector, η is the quantum efficiency of the photodetector, and e is the electron charge. At a wavelength of $\lambda = 850$ nm, a detector with $\eta = 100\%$ quantum efficiency will have a responsivity of $\Re = 0.69$ A/W. Typical Si and GaAs photodiodes achieve roughly $\Re = 0.5$ A/W, which we will use in example calculations below. The photocurrent also exhibits fluctuations characterized by the shot-noise formula

$$\Delta I^2 = 2BeI \ , \tag{3.5}$$

where I is the mean photocurrent and ΔI^2 is the mean-square value of photocurrent deviations from the mean. We note that the proof of equation (3.5) is not trivial. However, one can "derive" equation (3.5) by modeling a photodetector with efficiency η as an optical filter with power transmission coefficient η followed by an ideal photodetector with 100% efficiency.

Finally, the RIN as measured with a real photodetector is given by

$$RIN = \frac{1}{SNR \times B} , \tag{3.6}$$

where SNR is the photocurrent signal-to-noise ratio, defined by

$$SNR = \frac{I^2}{\Delta I^2} \ . \tag{3.7}$$

For a shot-noise-limited laser, we use the current fluctuations given by equation (3.5) to predict a detected RIN of

$$RIN_{SNL} = \frac{2e}{I} = \frac{3.2 \times 10^{-19} C}{I} \ . \tag{3.8}$$

For example, at I = 1 mA of photocurrent generated by a shot-noise-limited laser, we would measure a RIN = -155 dB/Hz. For a typical photodiode with responsivity $\Re$ = 0.5 A/W, this corresponds to an incident optical power of P = 2 mW at a wavelength of 850 nm. Although the detected RIN of a laser often exhibits "excess noise" that has some dependence on frequency, the result above says that the RIN due to shot noise alone is flat versus frequency. In fact, VCSELs have been shown to achieve shot-noise-limited RIN levels for output powers above roughly P = 1 mW.

We continue the example of the previous paragraph in order to determine the implications for analog transmission of signal from a FPA to a remote digitizer. We consider a readout rate of R = 10 Msample/s, which roughly translates into a bandwidth requirement of B = R = 10 MHz = 70 dB Hz. Hence, a RIN = -155 dB/Hz implies a photocurrent signal-to-noise ratio of SNR = 85 dB. The SNR of the input signal limits the number of bits *N* that can be accurately measured by an analog-to-digital converter according to

$$SNR = \left(2^N\right)^2 . \tag{3.9}$$

Equation (3.9) says that every bit of resolution requires 6 dB of SNR. Thus a SNR = 85 dB allows 14.2 bits of potential resolution by an input-noise-limited digitizer. A readout rate of R = 10 Msample/s with N = 14 bits of resolution is considered good performance for a cryogenic FPA.

We digress briefly to compare the scaling of analog versus digital transmission. For digital transmission, the required bandwidth is roughly equal to the bit rate, so that B = R×N, the product of the FPA readout rate R times the number of bits N of resolution, and the SNR determines the bit error rate (BER). For example, a BER = 1×10^{-10} requires a SNR = 22 dB, and the BER drops very rapidly with improved SNR. Hence, digital transmission with a BER = 1×10^{-10} requires a RIN below

$$RIN_D = \frac{1}{SNR \times B} = \frac{-22\text{dB}}{R \times N}, \tag{3.10}$$

where *R* is the readout rate, and *N* is the number of digitized bits per sample. For a readout rate of R = 10 Msample/s with N = 14 bits of resolution, R×N = 140 Mbit /s = 81.5 dB Hz, so that a RIN = –103.5 dB/Hz is required. Note that the RIN requirement of the digital system is much less demanding than for the similar analog system discussed above, which required a RIN = -155 dB/Hz.

For comparison with the digital RIN requirement of equation (3.10), we write an equation that shows how the required RIN scales for analog transmission

$$RIN_A = \frac{1}{SNR \times B} = \frac{1}{2^{2N} R}, \tag{3.11}$$

where again R is the readout rate, and N is the number of bits to be digitized per sample. Hence, at roughly N = 4 bits of resolution, the analog and digital systems are comparable in terms of their RIN requirements. However, if we want more than 4 bits of resolution, the demands on the RIN of an analog system scale much more rapidly than for the digital system. The demanding RIN requirements of analog transmission motivated us to consider digital transmission in the second year of the LDRD, as will be discussed in section 4. However, in the remainder of section 3, we will discuss our measurements pertaining to analog optical transmission of signals from a FPA to a remote digitizer.

3.3. Analog Transmission Experiments

The main goal for the first year of this LDRD was to set up and test an optical interconnect for transmitting analog signals from a FPA to a remote digitizer. Figure 3.1 shows a schematic layout of the entire setup, including the FPA, optical interconnect, and analog-to-digital converter. The FPA used for this demonstration was the Detector Array Readout Test (DART) chip, which requires only a clock signal and a 5-V DC power supply to operate. The DART output signal range is approximately 1.3 to 3.5 V. The silicon photodiode (PD) and transimpedance amplifier (TIA) are both part of the Thorlabs model PDA55 photodetector, which is discussed further in the next section. Finally, a level shift amplifier was used to translate the interconnect output voltage range to the –2 to +2-V range accepted by the GaGe model CS1012 analog-to-digital converter card.

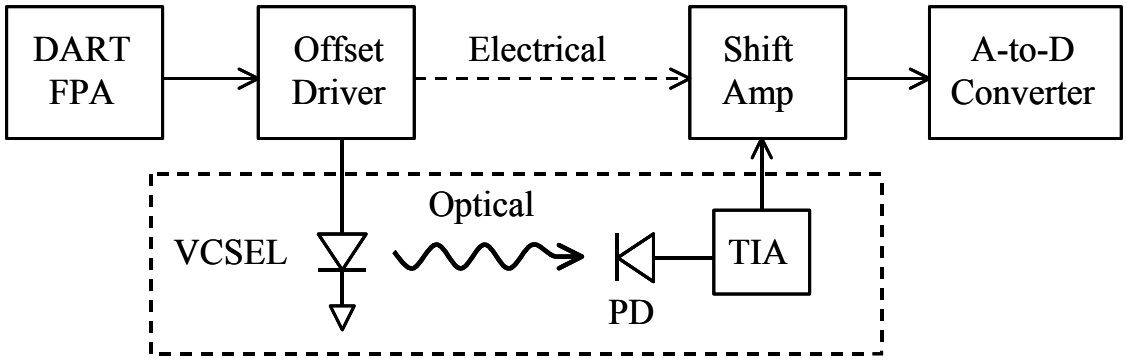

Figure 3.1. Schematic layout of the analog transmission experiment, including the DART FPA, optical interconnect, and analog-to-digital converter. We can bypass the optical interconnect, following the "Electrical" interconnect dashed line, in order to determine the noise contributed by the electronics only (without the optical interconnect). The silicon photodiode (PD) and transimpedance amplifier (TIA) are both part of the Thorlabs model PDA55 photodetector package.

The current and voltage requirements of the VCSEL are shown in figure 3.2, along with the optical output power produced by the VCSEL. Actually, the data shown in figure 3.2 are for the VCSEL wired to pin 5 of the package, whereas the VCSEL used in the actual demonstration was wired to pin 4 of the package. However, these two VCSELs are nominally identical. Notice that the DART output voltage range (1.3 to 3.5 V) is directly compatible with the VCSEL. However, since the VCSEL is really a current controlled device, we constructed a simple driver circuit to convert the DART voltage into a current drive for the VCSEL.

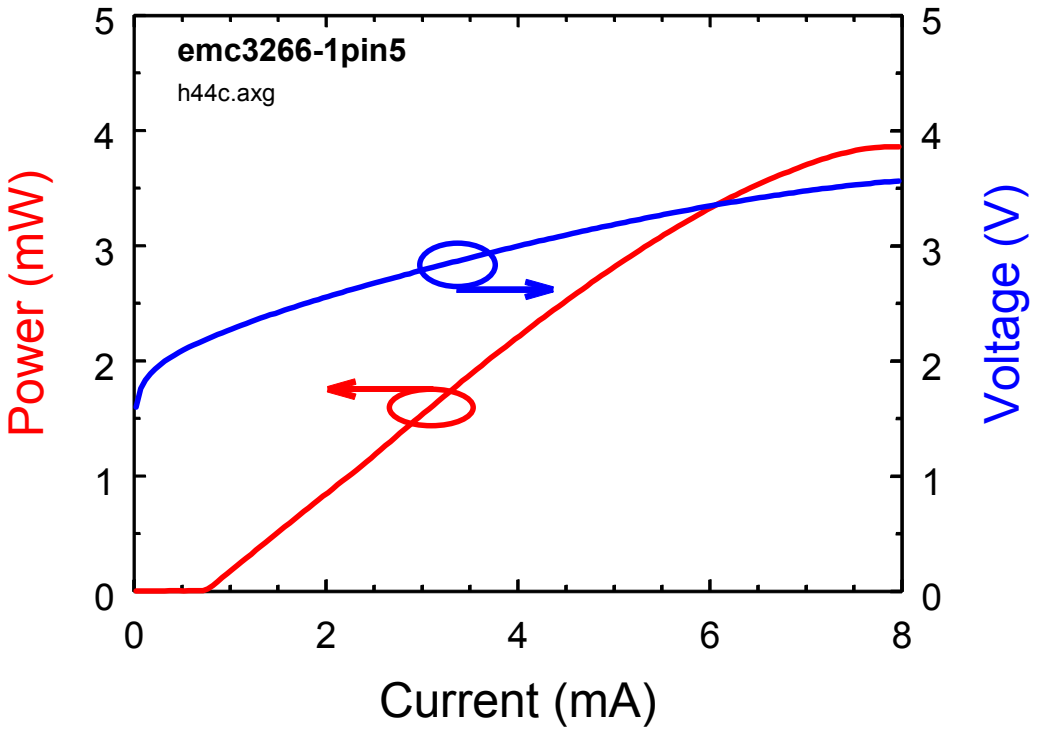

Figure 3.2. VCSEL output power and voltage drop versus drive current. The data are for wafer EMC3266, package # 1, pin 5. The actual laser used in the demonstration was nominally identical, but in fact was the VCSEL wired to pin 4.

Figure 3.3 shows a schematic diagram of the "offset driver" circuit that converts the FPA output voltage into a current to drive the VCSEL. The first amplifier stage provides an offset of the FPA output voltage according to the position of the 10-kohm potentiometer. The second stage amplifier provides a voltage gain G = 2.0 and drives the VCSEL through an output resistor R_O = 1000 ohm, which approximately converts voltage to current. The VCSEL voltage versus current data shown in figure 3.2 can be modeled as an ideal laser diode in series with a resistor R_S = 200 ohm (due to the distributed Bragg reflectors in the VCSEL structure). From threshold up to a few milliamperes above threshold, the voltage drop across the laser diode alone is V_D = 2.0 V. The current that drives the laser is given by $I_L = (2\times(V_F + V_O) - V_D) / (R_O + R_S)$, where V_F is the voltage output from the FPA and V_O is the effective offset voltage determined by the potentiometer setting. The potentiometer is experimentally adjusted so that the VCSEL is biased at threshold when the FPA output voltage is minimum. Assuming the laser diode voltage drop is approximately fixed at V_D = 2.0 V, the laser current increases as $\Delta I_L = 2\times\Delta V_F / (R_O + R_S) = \Delta V_F$ / 600 ohm. Hence, the FPA output voltage range of ΔV_F = 2.0 V yields a laser current modulation range of ΔI_L = 3.3 mA above threshold.

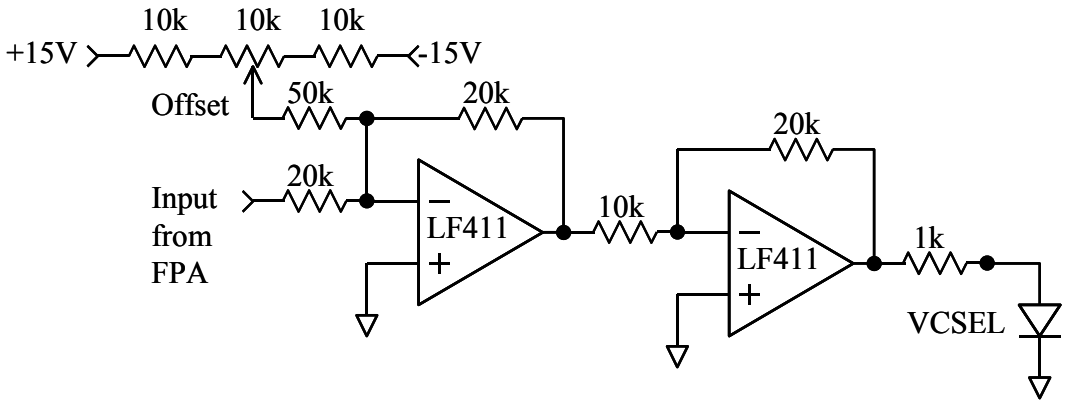

Figure 3.3. Schematic diagram of the "offset driver" circuit that converts the FPA output voltage into a current to drive the VCSEL. The first stage adds an offset to the input. The second stage provides a gain of 2. The output resistor (1k) approximately converts voltage to current.

Perhaps the most important result of the analog transmission experiment is that it worked surprisingly well. Although we generally expect such an analog optical interconnect to degrade the signal-to-noise ratio, we found that the degradation was only modest. Table 3.1 compares the data obtained for the optical interconnect versus that for the direct electrical interconnect. Notice that the "offset driver" circuit was used as part of the electrical interconnect experiment and it simply doubled the FPA output voltage range. The main reason to use the offset driver circuit in both interconnect experiments was to keep the electrical part of the two experiments the same.

Table 3.1. Comparison of signal and noise from electrical and optical interconnects.

Interconnect	Vmean	Vrms	Vmean / Vrms	SNR
Electrical	3.94 V	4.565 mV	864.1	58.7 dB
Optical	3.66 V	4.810 mV	760.4	57.6 dB

Although the DART FPA was designed to operate at readout rates up to 1 MHz, we chose to operate at a clock rate of 100 kHz, so that the signals fit comfortably within the bandwidth limits of the FPA output amplifier and the offset driver circuit. A GaGe model CS1012 12-bit analog-to-digital converter card was employed to capture and store 128 frames worth of data from the FPA. The DART chip actually contains 8 different 16-by-16-pixel arrays. Because of differences in the arrays, some output a low signal while others output a high signal, even in the dark. Our measurements were taken in the dark, using this feature of the DART chip. We determined the noise level by calculating the temporal root-mean-square voltage Vrms from one pixel in the high-output array A4. The signal level Vmean was determined by taking the difference in mean output voltages between the high-output array A4 and the low-output array A5. The data are summarized in table 3.1.

The overall noise for the optical interconnect case is expected to result from both electronic noise $N_E = V_{E,rms} / V_{E,mean}$ and optical noise $N_O = V_{O,rms} / V_{O,mean}$. Assuming

the two are uncorrelated, the total noise is found as the sum of squares: $N_T^2 = N_E^2 + N_O^2$. For the data given in table 3.1, $N_E = (864.1)^{-1}$ and $N_T = (760.4)^{-1}$. Taking the difference of the squares, we determine the optical noise contributed by the optical interconnect alone (VCSEL and photodetector) to be $N_E = (1600.9)^{-1}$, which yields an optical signal-to-noise ratio $SNR_O = 64.1$ dB. A SNR of 64.1 dB translates into 10.5 bits of potential resolution, based on the rule of equation (3.9) that every bit of resolution requires 6 dB of SNR.

The relatively high electrical noise levels observed in our analog transmission experiments limited our ability to accurately determine the limits imposed by the optical signal-to-noise ratio. In the following section, we describe a set of experiments that measures the optical signal-to-noise ratio more accurately.

3.4. Optical Noise Measurements

In this section, the noise of the VCSEL is quantified. The optical interconnect hardware, shown in the photograph in figure 3.4, includes the components contained within the dashed box in figure 3.1 (namely, a VCSEL, photodiode, and transimpedance amplifier). The GaAs VCSEL chip is mounted in a 16-pin ceramic package, and several of the VCSELs on the chip are wirebonded to separate pins on the package. The ceramic package is mounted sideways on an XYZ translation stage for ease in centering the VCSEL output beam on the photodiode. We used a Thorlabs model PDA55 photodetector, which contains a 3.6-mm-square silicon photodiode and a low-noise transimpedance amplifier.

In order to accurately measure the laser noise, care should be taken to insure that the photodetector noise is smaller than the optical noise to be measured. The optimum photodetector performance is obtained by using a photodiode with high quantum efficiency followed by a low-noise transimpedance amplifier. For moderate bandwidths, such low-noise photodetectors are available commercially. We selected a Thorlabs model PDA55 photodetector, which contains a silicon photodiode, with a responsivity of 0.55 A/W (80% quantum efficiency) at 850 nm, and a transimpedance amplifier, built with an Analog Devices AD829 high-speed low-noise op amp. The PDA55 provides a maximum bandwidth of 10 MHz at a transimpedance value of 15 kohm. The output of the PDA55 contains a 50-ohm series resistor, so that the output voltage is divided by 2 when the detector drives a 50-ohm load. The input referred current noise of the transimpedance amplifier is obtained as $i_T^2 = i_N^2 + (v_N / R_T)^2$, where i_N is the input current noise of the op amp, v_N is the input voltage noise of the op amp, and R_T is the transimpedance value. For the AD829, typical noise values are $i_N = 1.5$ pA/√Hz and $v_N = 1.7$ nV/√Hz at a frequency of 1 kHz. Hence, for a transimpedance of $R_T = 15$ kohm, the input referred current noise is $i_T = 1.5$ pA/√Hz. For comparison, equation (3.3) predicts a shot noise of 17.9 pA/√Hz with 1 mA of photocurrent. Since the laser is expected to have noise higher than the shot-noise limit, the PDA55 is perfectly adequate for measuring the laser noise.

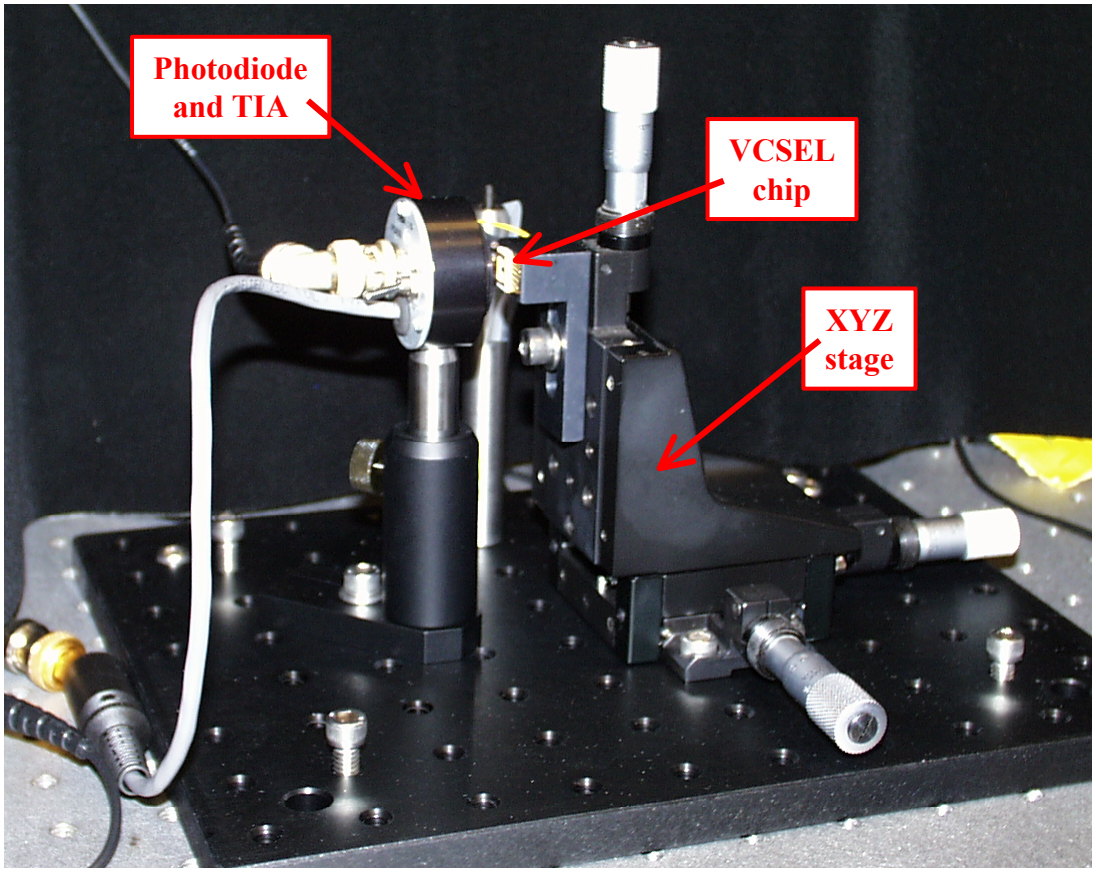

Figure 3.4. Photograph of the optical hardware that comprises the optical interconnect. The GaAs chip containing several VCSELs appears as a small black dot in the center of the white ceramic 16-pin package. The silicon photodiode (PD) and transimpedance amplifier (TIA) are both part of the Thorlabs model PDA55 photodetector.

The noise measurements were performed using a Hewlett-Packard 8562E spectrum analyzer (50-ohm input impedance) connected to the output of the PDA55 photodetector. Figure 3.5 shows both the VCSEL output optical power and the measured photodetector noise versus the current supplied to the VCSEL. The VCSEL was driven with a Keithley model 2400 DC current source. The spectrum analyzer was set up to measure the noise power in a 1-kHz resolution bandwidth at a center frequency of 50 kHz. The dashed curve in figure 3.5 shows the noise power that would have been detected if the photocurrent had been shot-noise limited. The VCSEL shows typical semiconductor laser behavior in which the shot-noise limit is approached as the drive current is increased well above threshold. We note that independent measurements, done with a lock-in amplifier, showed the photodetector electronic noise to be –115 dBm in a 1 kHz bandwidth. Hence, the noise measurement of –108 dB at I = 0 mA seems to be limited by the electronic noise of the spectrum analyzer itself.

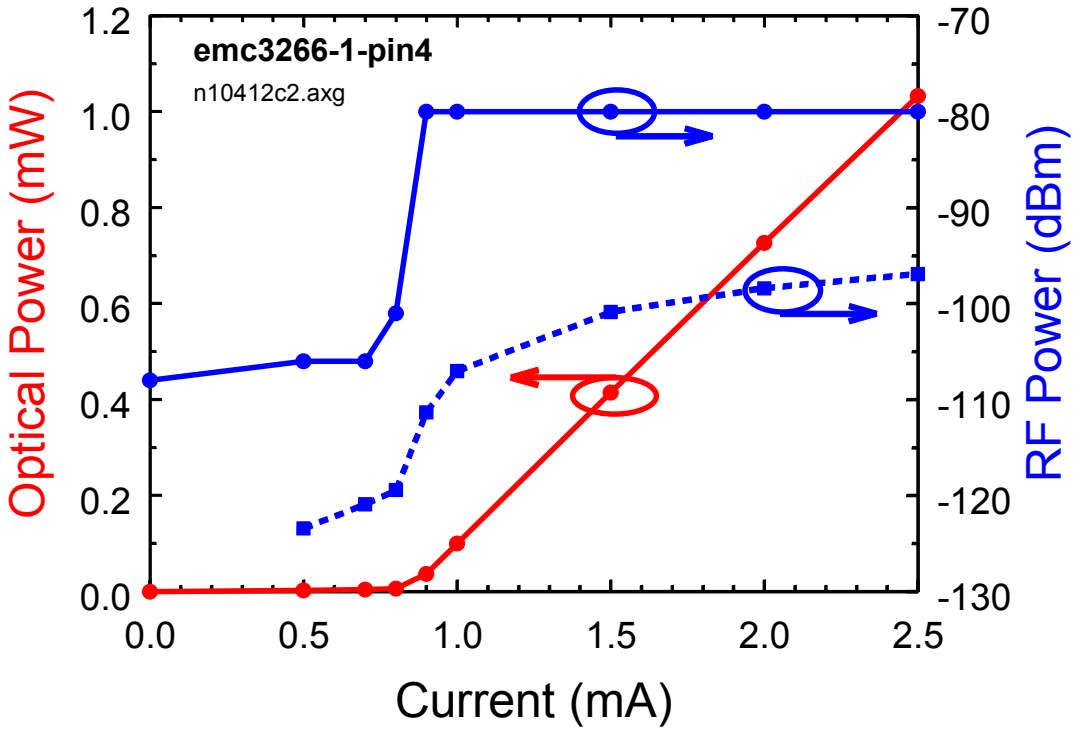

Figure 3.5. VCSEL optical power and photodetector output RF noise power versus VCSEL drive current. The RF power is measured in a 1-kHz resolution bandwidth at a center frequency of 50 kHz. For comparison, the dashed curve shows the RF power that would have been measured if the photocurrent had been shot-noise limited.

The RIN data, determined from the measurements described above, are plotted in figure 3.6. Clearly the RIN improves with increasing drive current, and also approaches the shot-noise-limited RIN for currents well above threshold. We note that shot-noise limited VCSELs have been previously demonstrated.[7] The VCSEL that we used attained a RIN of –135.6 dB/Hz at a drive current of 2.5 mA. The shot-noise-limited RIN corresponding to the same drive level was –152.5 dB/Hz, indicating that the VCSEL operated within 17 dB of the shot-noise limit.

The analog transmission experiments described in the previous section operated the VCSEL at a drive level near 2.5 mA, so we would expect a RIN near –135 dB/Hz. Assuming the bandwidth of the analog transmission experiments was roughly 1 MHz, we determine an optical signal-to-noise ratio of 75 dB. Although the analog transmission measurements implied an optical SNR of 64.1 dB, they were limited by electronic noise. However, it could be that low-frequency noise from the VCSEL and/or photodetector degrades the optical SNR somewhat from that determined above. Finally, we note that the observed laser RIN of –135 dB/Hz implies that it could support optical analog transmission from a FPA at a readout rate of 1 Mpixel/sec with 12.5 bits of resolution. Faster readout and/or more bits of resolution would require improving the VCSEL RIN toward the shot-noise limit.

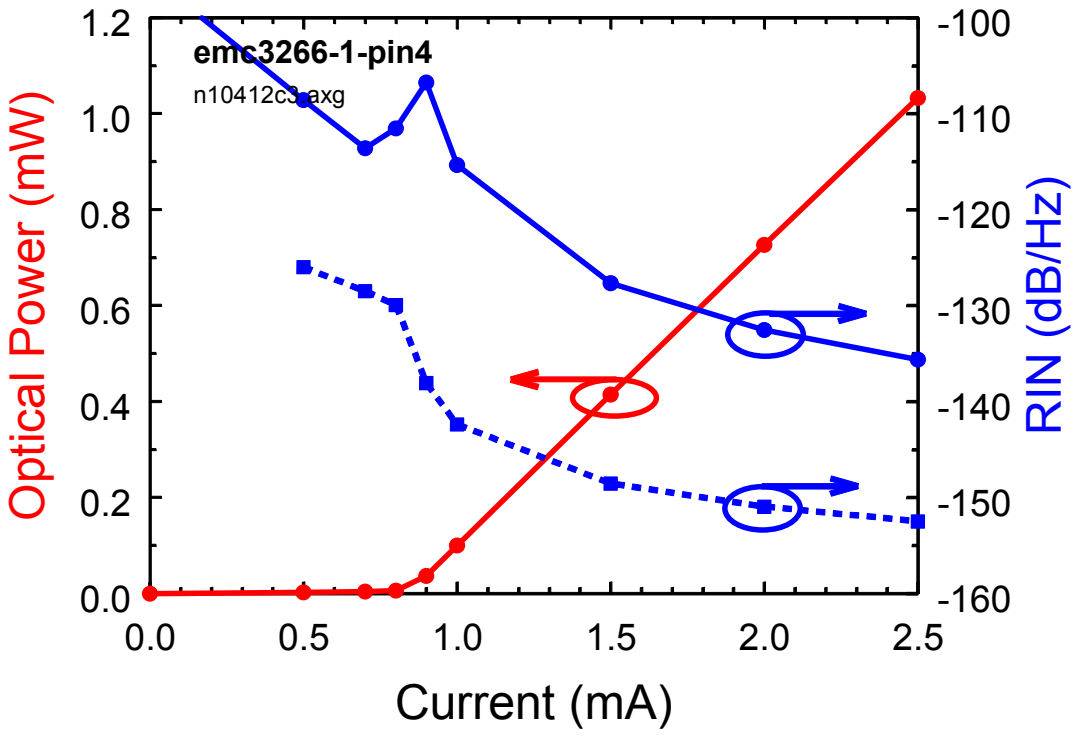

Figure 3.6. VCSEL optical power and detected relative intensity noise (RIN) versus drive current. For comparison, the dashed curve shows the RIN that would have been measured if the VCSEL had been shot-noise limited.

3.5. Analog Transmission Conclusions

In conclusion, we demonstrated that analog optical transmission of FPA signals to a remote digitizer, using a VCSEL, works reasonably well. In fact, our demonstration experiment was limited more by the electronic noise (from either the FPA or the analog-to-digital converter) than by the optical noise from the VCSEL. We used a test FPA operating at a readout rate of 100 kHz, and measured a digitized signal-to-noise ratio of 57.6 dB that was primarily limited by the electronic noise of the system.

In order to measure the optical noise of the VCSEL more accurately, we used a low-noise DC current driver to bias the VCSEL and a low-noise photodetector to convert the noise to the electronic domain where it was measured using a spectrum analyzer. With this system, we measured the relative intensity noise (RIN) of the VCSEL to be –135.6 dB/Hz at an output power of 1 mW. For comparison, the shot-noise limited RIN for the same detected photocurrent is calculated to be –152.5 dB/Hz, indicating that an improvement of 17 dB is possible. A goal for future work on analog optical interconnects would be to improve the RIN of the VCSEL to the shot-noise limit, which has previously been shown to be possible.

We have also theoretically considered the ultimate performance that could be achieved in an analog optical interconnect, limited only by shot noise. These calculations are valid for any optical transmission approach, using either direct or indirect modulation of lasers. One conclusion is that for 2 mW of optical power, corresponding to a shot-noise-limited RIN of –155 dB/Hz, analog optical readout of a FPA at a rate of 10 Mpixel/sec could be done with 14 bits of resolution. Other performance targets can be obtained by trading 1 bit of resolution to gain a factor of 4 in readout rate.

Finally, we have theoretically compared laser RIN requirements for analog versus digital transmission. The main conclusion is that an analog optical link is intrinsically more limited than a digital optical link, since the signal-to-noise ratio required for an analog link scales exponentially with the number of bits of resolution. The rapid scaling of RIN requirements for analog transmission motivated us to consider digital transmission in the second year of the LDRD, as will be discussed in the following section.

4. Digital Optical Transmission

4.1. Cryogenic Digital Transmission

In the second (final) year of this LDRD, we shifted our attention from analog to digital optical transmission. This shift was motivated mainly by our shot-noise calculations, discussed in section 3.2 above, which demonstrated that scaling to a higher number of bits of resolution is far easier to handle with digital optical transmission. Of course, this means that the optical interconnect must follow the analog-to-digital converter.

Although we had previously assumed that analog-to-digital converters would dissipate too much power to be cooled along with the FPA, recent advances in technology have yielded very low-power analog-to-digital converters that could be placed next to cryogenic FPAs. In this situation, one is again faced with the challenge of getting the data from the cryogenic circuitry to remote processing circuits.

If we can make efficient low-power cryogenic VCSELs, we could replace the metallic cables that bring digital data out of the cryostat with optical fibers, which are smaller and have lower thermal conductivity. Moreover, due to the low optical attenuation in the fibers, the data could be piped several meters to a remote computer, without the need for intermediate electronic receivers, serializers, and high-speed laser transmitters.

In addition to making the VCSELs operate well at low current and low temperature, it would be desirable if they could be driven directly from low-power CMOS logic levels, since conventional laser driver circuits consume much more power than the VCSEL itself. In taking this approach, we necessarily sacrifice some of the features of conventional laser driver circuits, which typically bias the lasers just above threshold to achieve high modulation bandwidth and automatically adjust the bias and drive current to compensate for ambient temperature changes. However, if the bit rate is kept below 1 Gbit/sec, such complicated laser biasing may not be required.

4.2. Cryogenic VCSELs

We designed, grew, fabricated and tested VCSELs that work from 100K to 300K. The pursuit of cryogenic VCSELs was new to us, but we knew that good performance from cooled VCSELs has been obtained elsewhere.[8,9]

The main design issue is the offset of the peak optical gain wavelength from the VCSEL cavity resonance. For 850-nm VCSELs operating at room temperature, the cavity resonance is set at $\lambda_{C0} = 850$ nm during the epitaxial growth, by controlling the layer thickness of the optical cavity (typically at one wavelength) and the distributed Bragg reflector (DBR) layers (at a quarter wavelength each). The peak optical gain wavelength is typically positioned at $\lambda_{G0} = 840$ nm, by controlling the thickness of the quantum wells that provide the gain. When the laser is operated, it heats locally due to the current injection and thus the VCSEL temperature rises. As the VCSEL temperature increases, the cavity resonance wavelength shifts at $d\lambda_C/dT = 0.06$ nm/K and the peak gain

wavelength shifts at $d\lambda_G/dT = 0.3$ nm/K.[10] Thus, a temperature rise of $\Delta T = (\lambda_{C0} - \lambda_{G0}) / (d\lambda_C/dT - d\lambda_G/dT) = 42$ K shifts the gain peak to overlap the cavity resonance at 852.5 nm. Such an intentional offset allows the VCSEL to operate better at elevated temperatures and elevated currents.

For cryogenic VCSELs, we must intentionally position the room-temperature cavity resonance at a wavelength considerably shorter than the peak gain wavelength. We decided to keep our quantum wells the same, so that the peak gain wavelength remained at $\lambda_{G0} = 840$ nm, but we shifted the room-temperature cavity resonance to $\lambda_{C0} = 825$ nm. In this case, we expect the two wavelengths to merge at $\Delta T = -62.5$ K from room temperature, or in other words at about 233 K in absolute temperature. In reality, the temperature coefficients are somewhat smaller below room temperature, so the expected optimum temperature is more towards 200 K. Figure 4.1 shows the measured threshold current versus ambient temperature, which confirms that the lowest threshold current (0.66 mA) is obtained at 200 K.

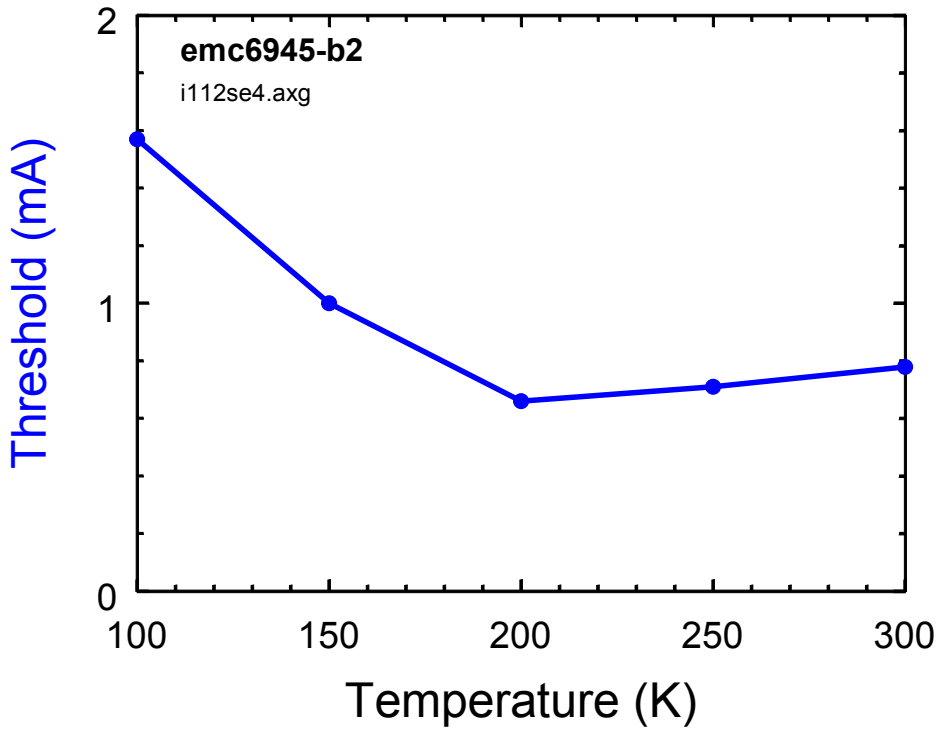

Figure 4.1. Cryogenic VCSEL threshold current versus absolute temperature.

Figures 4.2 and 4.3 show the output optical power and drive voltage, respectively, versus drive current for a cryogenic VCSEL. In addition to the threshold current reaching a minimum at 200K, the other salient features are the increase in slope efficiency, maximum output power, and drive voltage as the temperature is reduced.

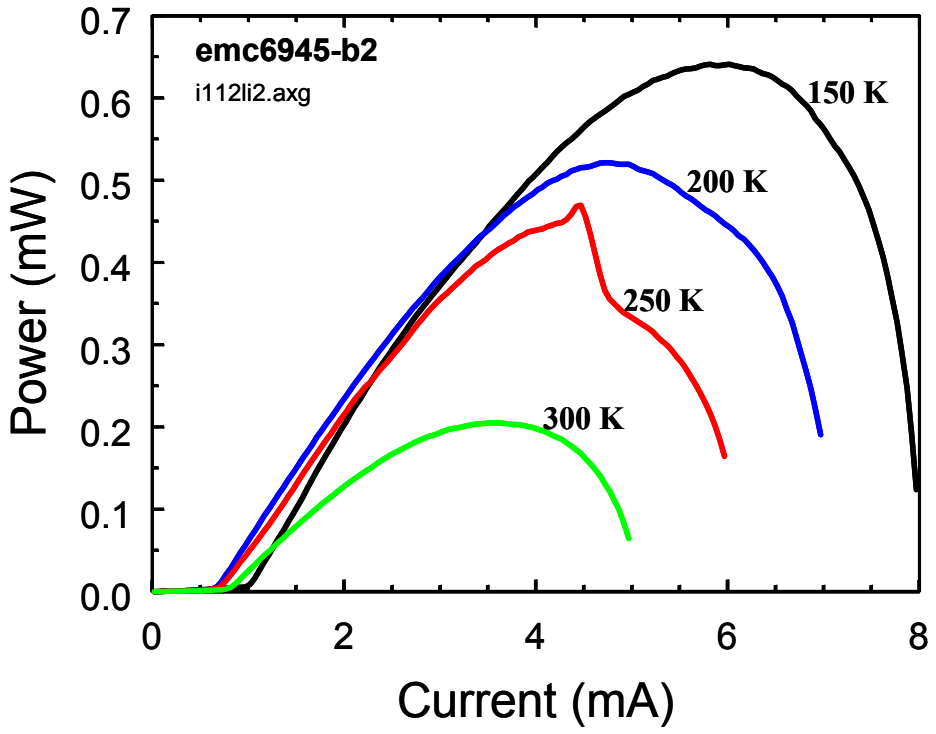

Figure 4.2. Cryogenic VCSEL power versus current data at various temperatures.

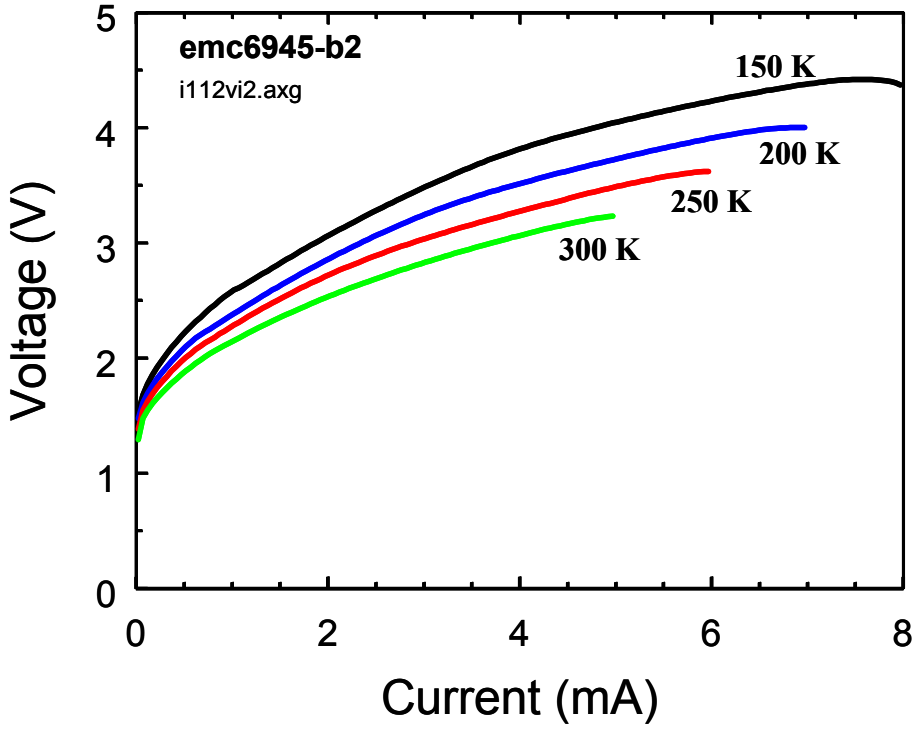

Figure 4.3. Cryogenic VCSEL voltage versus current data at various temperatures.

Figure 4.4 shows the drive voltage and slope efficiency versus ambient temperature. One of our main concerns in making cryogenic VCSELs is dopant freeze-out at low temperatures leading to a significant increase in series resistance and hence the drive voltage. However, for wafer emc6945, we used our standard VCSEL doping levels to see if they would be adequate. Figure 4.4 plots the voltage drop at 1 mA of drive current, and shows that it increases from 2.16 to 2.86 V as the temperature is lowered from 300 to 100 K. The good news is that the voltage increase is not as severe as we thought it might be. Furthermore, we note that some of this voltage increase can be accounted for as an inevitable consequence of the bandgap change with temperature. The bandgap contribution to the drive voltage will not be an issue if we design the VCSEL to operate at 850 nm at cryogenic temperatures. Finally, we observe that the slope efficiency steadily increases as the temperature is lowered. This is expected, since the free-carrier absorption will be reduced at lower temperatures.

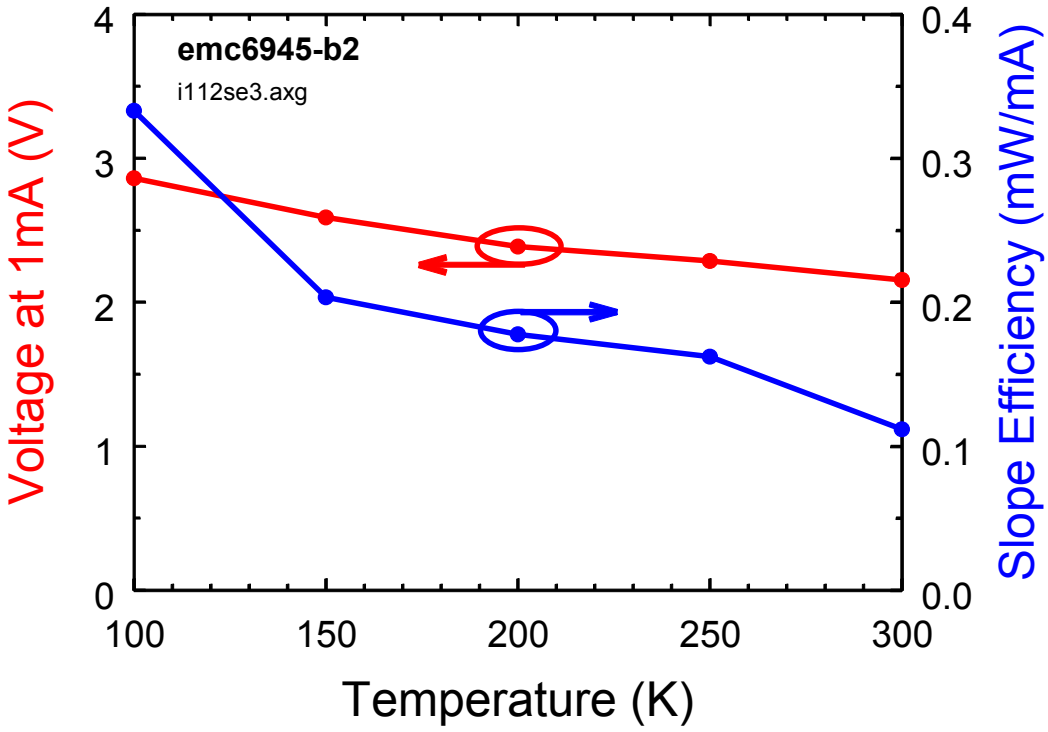

Figure 4.4. Cryogenic VCSEL voltage at 1 mA of drive current and slope efficiency versus absolute temperature.

Although our first cryogenic VCSELs were not perfectly optimized, they demonstrate that simple design changes allow us to obtain VCSELs that work at cryogenic temperatures. The optimization of the doping concentrations for cryogenic operation is a topic that should be investigated further. Also, in the future, we should consider using InGaAs instead of GaAs quantum wells for two reasons: (1) to get the proper gain offset so that the VCSEL works well at 850 nm at cryogenic temperatures, and (2) to take advantage of the reduced transparency current density in InGaAs quantum wells to achieve lower threshold currents.

4.3. Driving VCSELs with Low-Power CMOS Circuits

In order to minimize power dissipation in the cryostat, it would be best to omit the conventional laser driver circuits and instead drive the VCSELs directly with the output of the low-power CMOS logic circuit at the output of the analog-to-digital converter. In order to be successful, we must ensure that the VCSEL current and voltage requirements are compatible with the CMOS drive capability. Figure 4.5 shows the optical power and voltage characteristics of a typical low-power VCSEL versus drive current. In particular, we note that the threshold current is 0.5 mA and the threshold voltage is 1.88 V. Also, at a drive current of 1.0 mA, the voltage is 2.15 V, the output optical power is 0.4 mW, and the dissipated power is 1.75 mW.

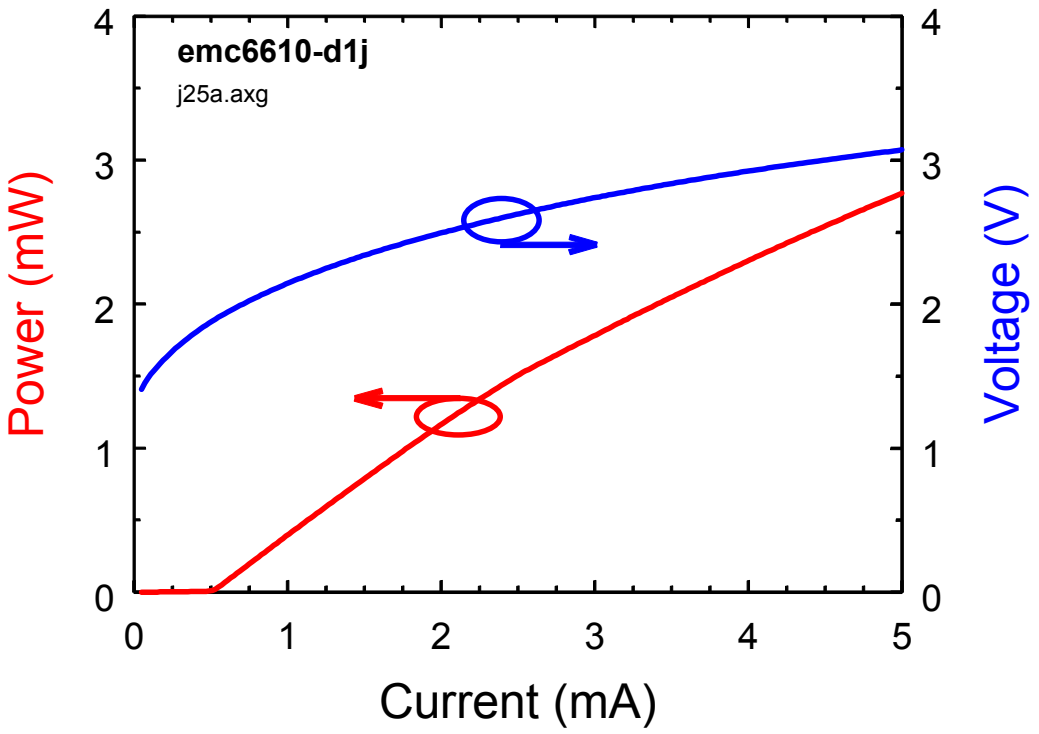

Figure 4.5. Output power and laser voltage versus drive current for the low-power VCSEL selected to be driven by an advanced low-voltage CMOS logic circuit.

We selected the advanced low-voltage CMOS (ALVC) family of circuits from Texas Instruments to drive our VCSELs, because this family provides both low power dissipation and high-speed performance. Specifically, we decided to use a Schmitt-trigger inverter chip (model SN74ALVC14) driven by a sine wave from a radio-frequency (RF) signal generator, as indicated in figure 4.6. The SN74ALVC14 chip is designed to operate from a power supply voltage of 2.3 to 3.6 V, and it can source or sink up to 24 mA when used with a 3-V supply. The output resistance is less than 50 ohms. Finally, when driving an output load of 500 ohms in parallel with 50 pF, the manufacturer has measured typical rise and fall times of 2.3 ns. Roughly, these rise and fall times suggest that the chip should operate up to a frequency of about 100 MHz.

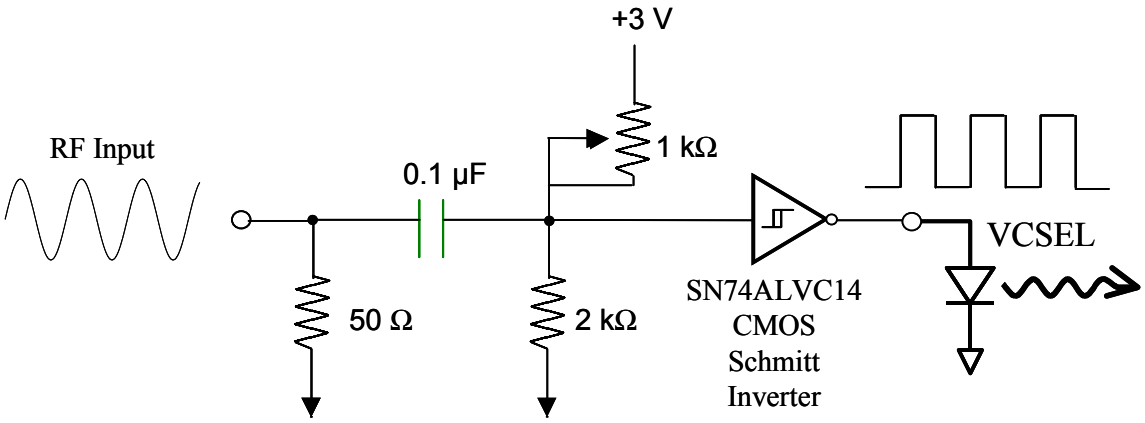

Figure 4.6. Schematic diagram of the electrical circuit used to drive the VCSEL. The input sine wave is obtained from a radio-frequency (RF) signal generator, and the 1-kohm potentiometer is used to shift the DC input to match the CMOS switching threshold levels.

Figure 4.6 shows an electrical circuit diagram of the setup used to drive the VCSEL with the SN74ALVC14 CMOS chip. Photographs of the circuit and VCSEL chip are shown in figures 4.7 and 4.8, respectively. We note that the VCSEL chip shown contains over 50 separate VCSELs, but only a few VCSELs were wirebonded to the pins of the TO can.

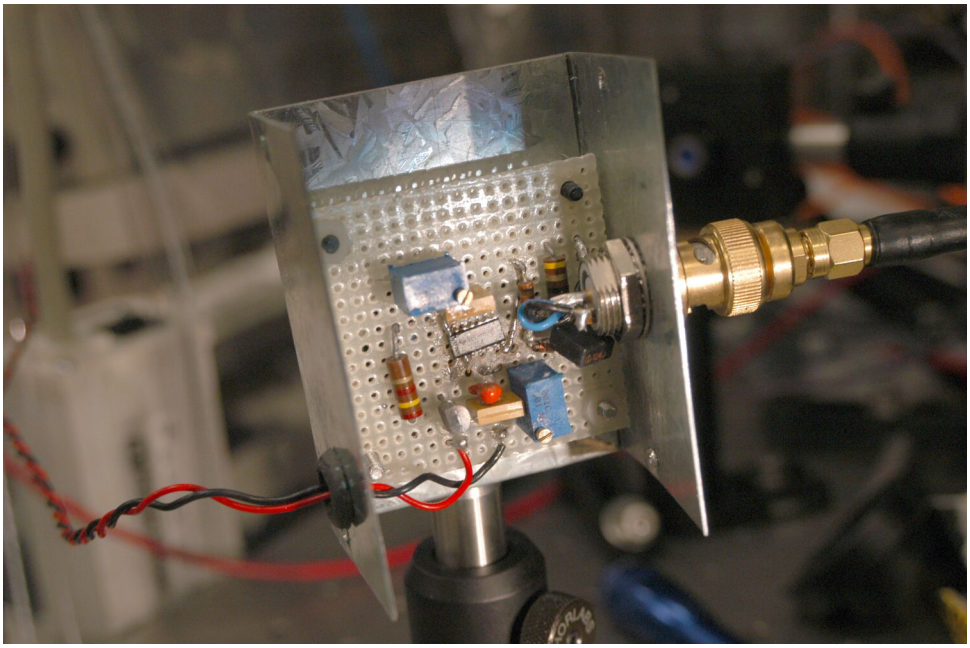

Figure 4.7. Photograph of the electrical circuit used to drive the VCSEL. The SN74ALVC14 is the small black 14-pin chip in the center of the circuit board. The upper blue potentiometer adjusts the supply voltage regulator and the lower blue potentiometer adjusts the DC level at the input to the SN74ALVC14.

The output light from the VCSEL was focused into an optical fiber, which was connected to a high-speed photodetector. Initially, we took DC measurements (omitting the RF input) to determine the CMOS output voltage and current levels. Specifically, we provided a 2.75-V supply to the SN74ALVC14 chip and biased the input to achieve a high output logic level. In this case, we measured 1.5 mW of optical power from the VCSEL, which implies (from the data in figure 4.5) an electrical input to the VCSEL of 2.5 mA at 2.62 V.

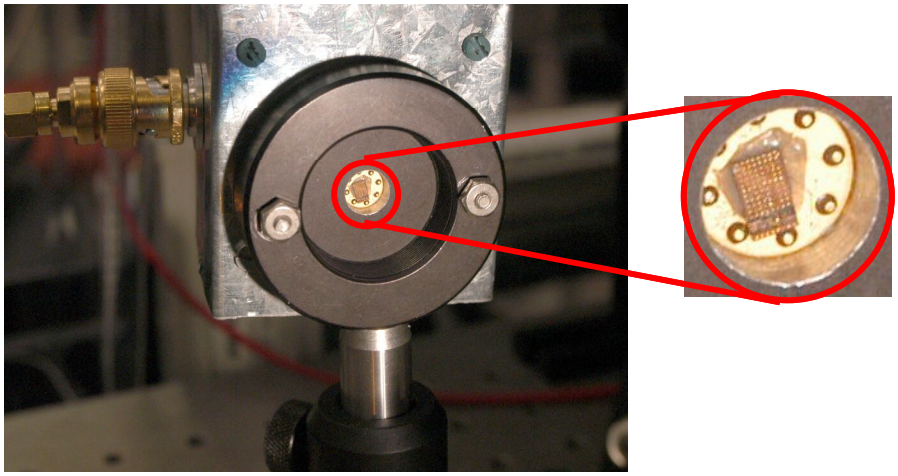

Figure 4.8. Photograph of the VCSEL chip, mounted in a TO can attached to the back side of the circuit board shown previously. Note that there are over 50 separate VCSELs on this GaAs chip, but only a few are wirebonded to the available pins of the TO package.

We tested the AC switching performance of the SN74ALVC14 CMOS chip over a range of frequencies from 1 MHz to beyond 200 MHz. Although the circuit worked equally well with supply voltages of 2.75 and 3.0 V, the data reported below was measured using a supply voltage of 3.0 V. Figure 4.9 shows an input sine wave at 5 MHz and the resulting output voltage waveform from the SN74ALVC14 CMOS chip, as measured with a Tektronix P6201 FET probe having an input impedance of 1 Mohm in parallel with 1.5 pF. The observed overshoot and ringing of the output voltage are most likely due to the circuit not being fabricated specifically to achieve optimum high-frequency performance. For example, a ground plane was not used. However, as indicated by the waveform in figure 4.9, the ringing decays largely within 25 ns and completely within 100 ns of the switching transition. Although the data in figure 4.9 was obtained while the VCSEL was hooked up and operating, we also tested the circuit with a 1-kohm load, and observed virtually identical ringing without the VCSEL or the capacitance of the probe involved. We therefore conclude that the ringing is mainly due to the circuit board layout and the intrinsic performance of the CMOS chip, rather than being due to the VCSEL loading. For reference, the VCSEL load appears approximately as a 200-ohm resistor in series with an ideal laser diode. The total parasitic parallel capacitance is less than 1 pF, and the parasitic series inductance is dominated by the wirebond length of roughly 3 mm and the TO can lead length of roughly 8 mm. For this application, the parasitic inductance is expected to be the most serious factor, but it is still relatively insignificant

compared to the intrinsic performance of the CMOS chip and the layout of the circuit board.

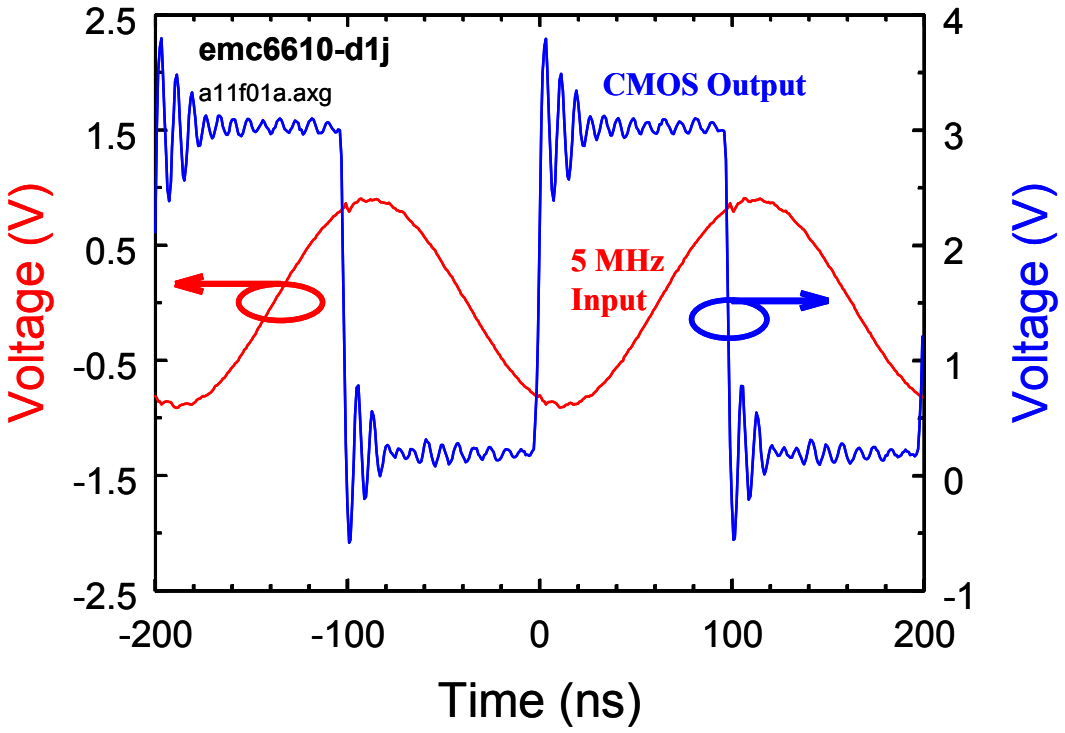

Figure 4.9. Input sine wave at 5 MHz and the resulting output voltage trace from the SN74ALVC14 CMOS chip, as measured with a Tektronix P6201 probe having an input impedance of 1 Mohm in parallel with 1.5 pF. Although the VCSEL was hooked up and operating during these measurements, essentially identical output waveforms were observed with a pure 1-kohm resistive load instead of the VCSEL.

Figure 4.10 shows the output optical waveform resulting from the CMOS waveform driving the VCSEL at 5 MHz. The observed 9-ns delay, from the CMOS output rising edge to the VCSEL output rising edge, is dominated by the propagation delays associated with the coaxial cables and optical fibers employed in the measurement. We used a Thorlabs model DET210 1-mm-diameter silicon photodiode driving the 50-ohm input of a Tektronix TDS3054B oscilloscope for these measurements. The risetime of the DET210 driving a 50-ohm load is specified to be 1 ns, corresponding to an RC-limited bandwidth of roughly 300 MHz. Notice that the VCSEL output faithfully reproduces the ringing produced by CMOS output, and in fact even magnifies it slightly due to the sensitivity of the VCSEL output power to input voltage variations.

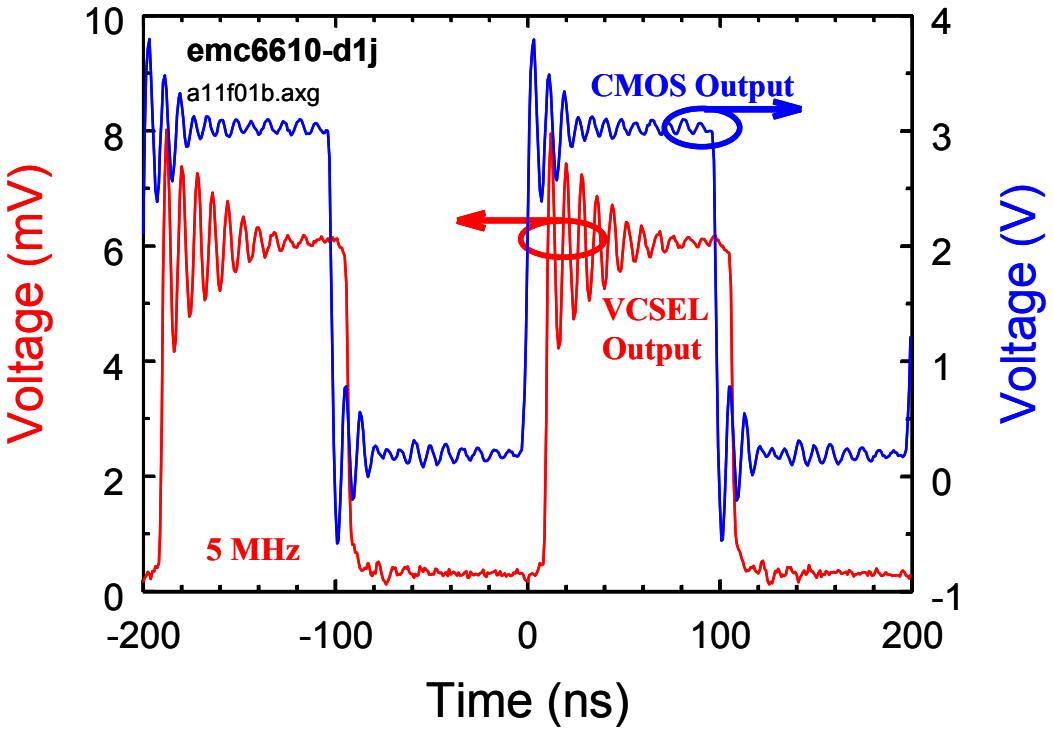

Figure 4.10. The VCSEL output waveform (left axis) resulting from the CMOS drive waveform (right axis) at 5 MHz. The roughly 9-ns relative delay of the VCSEL waveform results from propagation delays in the coaxial cables and optical fibers.

Figure 4.11 shows the output optical waveform resulting from the CMOS waveform driving the VCSEL at 50 MHz. In order to clearly show the cause and effect, we have shifted the time axis of the VCSEL waveform by 9 ns to account for the cable delays in the measurement setup. The AC waveforms are dominated by the first cycle of the ringing, which appeared clearly in the 5-MHz data. Again, the VCSEL essentially follows the variations in the drive waveform. The slight differences are most likely due to either the fidelity of our voltage probe measurements or the circuit board layout yielding differences between the voltages at the CMOS output pin and those at the VCSEL bondpads.

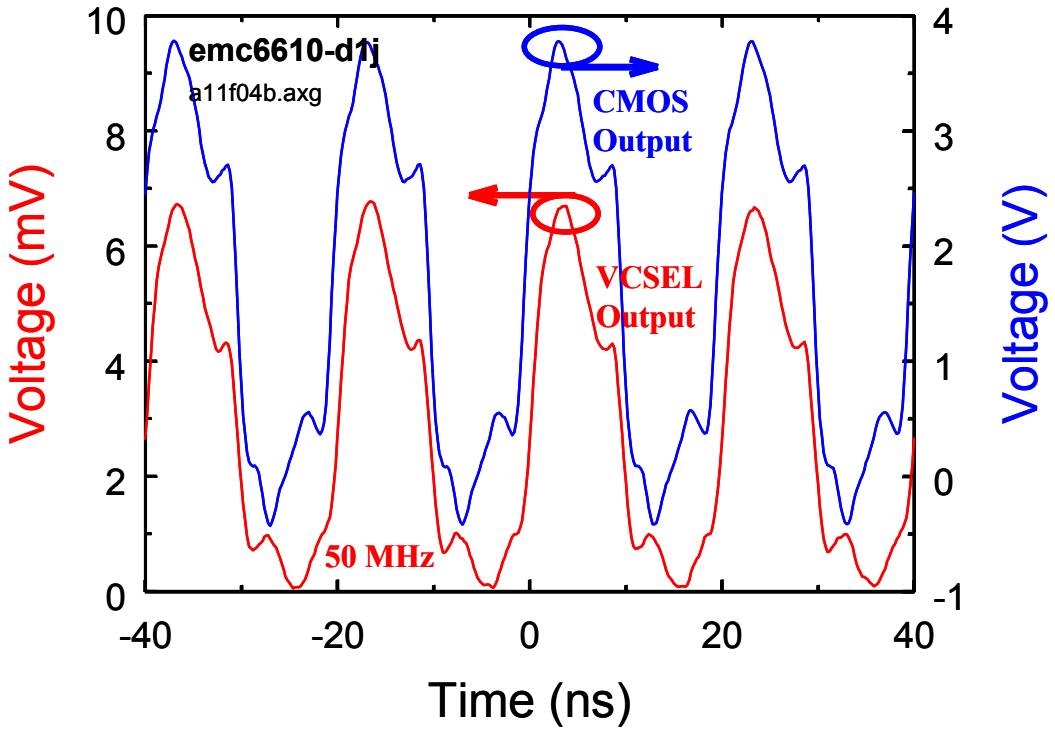

Figure 4.11. The VCSEL output waveform (left axis) resulting from the CMOS drive waveform (right axis) at 50 MHz. The time axis of the VCSEL waveform has been shifted by 9 ns to account for the cable delays in the measurement setup.

The main conclusion here is that the VCSEL electrical drive requirements and loading characteristics are compatible with direct driving by low-power CMOS circuits. Although we drove the VCSEL at roughly 3.3 mA and 2.8 V for the high-speed measurements reported above, this VCSEL would likely work with as little as 1.0 mA and 2.15 V. In the future, it is conceivable that the CMOS supply voltage could be reduced to as little as 1.0 V. Although a 1.0-V supply might appear hopeless for driving VCSELs with a bandgap of 1.4 V, a simple solution would be to return the VCSEL cathode to a –1.5 V DC supply line. The point is that only a 1.0-V swing (or less) is needed to drive the VCSEL between threshold and high output states. Providing the additional negative supply rail is a relatively easy thing to do using low-power solid-state DC to DC converter circuits.

4.4. Digital Transmission Conclusions

In the second year of this LDRD, we designed, grew, fabricated, and tested low-power-dissipation cryogenic VCSELs intended to be driven directly by the output stages of low-power CMOS analog-to-digital converters situated next to a cooled FPA. The VCSELs operated over a temperature range from 100 to 300 K. At 200K we measured a threshold current of 0.66 mA and a threshold voltage of 2.2 V, which translates into a threshold power dissipation of 1.45 mW. We expect that with further optimization the threshold

power dissipation of a cryogenic VCSEL could be reduced below 1 mW. We also observed that slope efficiency increased as the temperature was lowered. Importantly, the voltage drop across the VCSEL did not start to rise dramatically until the temperature was lowered below 100K, which implies that conventional doping concentrations can be used for VCSELs operating down to about 100K.

We also demonstrated that low-power VCSELs can be driven directly with low-power CMOS circuits by using a commercial SN74ALVC14 CMOS inverter chip to drive a VCSEL. At a supply voltage of 2.75 V, we measured a VCSEL output power of 1.5 mW, corresponding to a drive level of 2.5 mA at 2.62 V. High-speed switching operation was characterized to beyond 200 MHz, but square wave overshoot and ringing that decayed in roughly 25 ns limited our ability to quantify the ultimate bandwidth limitations of the CMOS-driven VCSEL. We determined that the observed ringing was mainly a result of either the circuit board layout (without a ground plane) or the intrinsic limitations of the CMOS chip that we used (the manufacturer reports a rise time of 2.3 ns and overshoot above 10%). Nevertheless, based on our data, the VCSEL appears to faithfully reflect the electrical drive waveform to within 2 ns of temporal resolution.

5. Summary

During this two-year LDRD, we have investigated the potential of optical interconnects for transmitting data from focal-plane arrays (FPAs) to remote processing electronics on board a satellite. For future FPAs, the higher bandwidths required for data readout may necessitate optical rather than electronic transmission. Compared to a coaxial cable, an optical fiber offers high bandwidth capacity, low attenuation coefficient, immunity to electromagnetic interference, and substantial savings in both size and weight.

We have focused mainly on low-power optical transmitters that could be located in a cryostat along with a cooled FPA. Due to the difficulty of keeping the FPA and associated electronics cold, it is important to minimize the power dissipated as heat. In order to be competitive with electronic transmitters, a reasonable goal is to keep the power dissipation of the optical transmitters below 5 mW each. Comparing potential laser diode transmitters, we observe that vertical-cavity surface-emitting lasers (VCSELs) dissipate roughly 10 times less power than edge-emitter lasers (EELs). Alternatively, we also considered using either an electro-absorption modulator (EAM) or an electro-optic modulator (EOM) to modulate the power of a laser located outside of the cryostat. The primary drawbacks to using optical modulators are that they increase the system complexity and typically exhibit nonlinear transfer functions. In terms of power efficiency, both EAMs and EOMs are potentially competitive with electrically modulated diode lasers. We conclude that the VCSEL is the best overall choice, for low power dissipation, linear transfer function, and ease of implementation.

In the first year of this LDRD, we concentrated on the task of transmitting analog signals from a cryogenic FPA to a remote analog-to-digital converter. We used a VCSEL to transmit analog signals from a test FPA to a remote digitizer. The demonstration worked well and was mainly limited by the noise of the test FPA electronics and/or the digitizer. We set up a separate experiment in which we accurately measured the relative intensity noise (RIN) of the VCSEL to be –135.6 dB/Hz at an output power of 1 mW, which is within 17 dB of the shot-noise limit.

We also theoretically compared laser RIN requirements for analog versus digital transmission. The main conclusion was that an analog optical link is intrinsically more limited than a digital optical link, since the signal-to-noise ratio required for an analog link scales exponentially with the number of bits of resolution. The rapid scaling of RIN requirements for analog transmission motivated us to consider digital transmission in the second year of the LDRD.

In the second year of this LDRD, we designed, grew, fabricated, and tested low-power-dissipation cryogenic VCSELs intended to be driven directly by the output stages of low-power CMOS analog-to-digital converters situated next to a cooled FPA. We validated our design approach and determined that conventional doping concentrations are adequate for temperatures down to 100 K. We also demonstrated that low-power VCSELs can be driven directly with low-power (3-V power supply) CMOS logic circuits, eliminating the need for conventional laser driver circuits that typically consume

large amounts of power. Finally, we noted that the VCSEL could be driven by future CMOS circuits with power supply voltages as low as 1 V simply by providing an additional negative DC power supply line for the VCSEL cathode. Further work remains to be done to accurately determine the maximum data rates that can be achieved by directly driving VCSELs with low-power logic circuits.

6. References

[1] L.A. Coldren and S.W. Corzine, Diode Lasers and Photonic Integrated Circuits, Wiley, New York (1995).

[2] J. Singh, Semiconductor Optoelectronics: Physics and Technology, McGraw-Hill, New York (1995).

[3] A. Yariv, Optical Electronics, 4th ed., Saunders, Philadelphia (1991).

[4] J.L. Rienstra and M.K. Hinckley, "Optical interconnections to focal plane arrays," SAND report SAND2000-2882, Sandia National Laboratories, Albuquerque (2000).

[5] A. Yariv, Chapter 10, "Noise in Optical Detection and Generation," in Optical Electronics, 4th ed., Saunders, Philadelphia (1991).

[6] A. Yariv, p. 437, Optical Electronics, 4th ed., Saunders, Philadelphia (1991).

[7] D. Wiedenmann, P. Schnitzer, C. Jung, M. Grabherr, R. Jager, R. Michalzik, and K.J. Ebeling, "Noise characteristics of 850 nm single-mode vertical cavity surface emitting lasers," Appl. Phys. Lett., vol. 73, pp. 717 – 719 (1998).

[8] B. Lu, W.-L. Luo, C. Hains, J. Cheng, R.P. Schneider, K.D. Choquette, K.L. Lear, S.P. Kilcoyne, and J.C. Zolper, "High-Efficiency and High-Power Vertical-Cavity Surface-Emitting Laser Designed for Cryogenic Applications," IEEE Photon. Technol. Lett., vol. 7, pp. 447 – 448 (1995).

[9] B. Lu, Y.-C. Lu, J. Cheng, R.P. Schneider, J.C. Zolper, and G. Goncher, "Gigabit-per-Second Cryogenic Optical Link Using Optimized Low-Temperature AlGaAs-GaAs Vertical-Cavity Surface-Emitting Lasers," IEEE J. Quantum Electron., vol. 32, pp. 1347 – 1359 (1996).

[10] B. Tell, K.F. Brown-Goebeler, R.E. Leibenguth, F.M. Baez, and Y.H. Lee, "Temperature dependence of GaAs-AlGaAs vertical cavity surface emitting lasers," Appl. Phys. Lett., vol. 60, pp. 683 – 685 (1992).

DISTRIBUTION:

1	MS	1077	T. E. Zipperian, 1740
6	MS	0603	D. K. Serkland, 1742
2	MS	0603	C. T. Sullivan, 1742
2	MS	0603	K. M. Geib, 1742
2	MS	0603	E. L. Blansett, 1742
1	MS	0603	G. D. Karpen, 1742
1	MS	0603	G. M. Peake, 1742
1	MS	0972	C. A. Boye, 5710
1	MS	0972	K. R. Lanes, 5715
1	MS	0971	A. J. Medina, 5730
2	MS	0972	J. L. Rienstra, 5731
1	MS	0188	LDRD Program Office, 1030
1	MS	9018	Central Technical Files, 8945-1
2	MS	0899	Technical Library, 9616
1	MS	0612	Review & Approval Desk, 9612 For DOE/OSTI